minerals

MDPI

Article

Geochemistry of Tourmaline from the Laodou Gold Deposit in the West Qinling Orogen, Central China: Implications for the Ore-Forming Process

Xiaoye Jin [1,2,3,*] and Jixiang Sui [4]

1 School of Earth Resources, China University of Geosciences, Wuhan 430074, China
2 State Key Laboratory of Geological Processes and Mineral Resources, China University of Geosciences, Wuhan 430074, China
3 Engineering Technology Innovation Center of Mineral Resources Explorations in Bedrock Zones, Ministry of Natural Resources, Guiyang 550081, China
4 Yifu Museum, China University of Geosciences, Wuhan 430074, China; suijx@cug.edu.cn
* Correspondence: xiaoye.jin@cug.edu.cn

Received: 26 June 2020; Accepted: 20 July 2020; Published: 22 July 2020

Abstract: The Laodou gold deposit, located in the West Qinling Orogen of central China, is a newly recognized intrusion-related gold deposit. It consists of auriferous quartz-sulfide-tourmaline and minor quartz-stibnite veins that are structurally controlled by fault zones transecting the host quartz diorite porphyry. Two types of tourmaline were identified in this study: Type 1 tourmaline occurs as quartz-tourmaline nodules within the quartz diorite porphyry, whereas type 2 tourmaline occurs as quartz-sulfide-tourmaline veins in auriferous lodes. Here, we present a major and trace element analysis by electron microprobe and laser ablation inductively coupled plasma mass spectrometry on these two types of tourmaline. Both tourmaline types fall into the alkali group, and are classified under the schorl-dravite solid solution series. The substitutions of $FeMg_{-1}$, $FeAl_{-1}$, $AlO((Fe, Mg)(OH))_{-1}$, and X-site $vacancyCa_{-1}$ are inferred by the variations of their major element compositions. Field and mineralogy observations suggest that type 1 tourmaline is a product of the late crystallization process of the quartz diorite porphyry, whereas type 2 tourmaline coexists with Au-bearing arsenopyrite and is crystallized from the ore-forming fluids. Their rare earth element compositions record the related magmatic hydrothermal evolution. The Co and Ni concentrations of the coexisting type 2 tourmaline and arsenopyrite define a regression line (correlation coefficient = 0.93) with an angular coefficient of 0.66, which represents the Co/Ni ratio of the tourmaline and arsenopyrite-precipitating fluids. This value is close to the Co/Ni ratios of the host quartz diorite porphyry, indicating a magma origin of the ore-forming fluids. The substitution of Al^{3+} by Fe^{3+} in both tourmaline types shows that type 1 tourmaline approaches the end member of povondraite whereas type 2 tourmaline occurs in opposite plots near the end member of Oxy-dravite, reflecting a more oxidizing environment for type 2 tourmaline formation. Moreover, the redox-sensitive V and Cr values of type 2 tourmaline are commonly 1–2 orders of magnitude higher than those of type 1 tourmaline, which also suggests that type 2 tourmaline forms from more oxidizing fluids. Combined with gold occurrence and fluid properties, we propose that the increasing of oxygen fugacity in the ore-forming fluids is a trigger of gold precipitation.

Keywords: tourmaline; geochemistry; ore-forming process; Laodou gold deposit; West Qinling Orogen

1. Introduction

Tourmaline is common in a variety of hydrothermal ore deposits such as granite related W–Sn polymetallic mineralization [1–3], porphyry Cu ± Mo [4,5], orogenic gold [6–8], volcanic-hosted

massive sulfide [9–11], and iron oxide–copper–gold deposits [12–14]. These diverse deposit types cover a broad spectrum of chemical environments and pressure-temperature conditions, suggesting a wide stability range for tourmaline [15]. This mineral phase is a borosilicate with large variations in chemical composition, containing most of the rock-forming elements and a certain number of volatile components (e.g., B, F, and OH) intrinsic to hydrothermal systems [16]. Chemical compositions and changes in tourmaline textures may provide evidence for changes in the process related to the crystallization history, and with proper decoding can elucidate the chemical evolution of the hydrothermal system [17,18].

Previous studies have shown that selected major and trace element compositions of tourmaline in hydrothermal deposits can be used as good indicators for the source and evolution of ore-forming fluids [19–21]. In this study, we present an in-situ dataset on major and trace element compositions of two types tourmaline from a newly recognized intrusion-related Laodou gold deposit in the West Qinling Orogen of central China. This gold deposit is characterized by an abundance of tourmaline occurring within the host quartz diorite porphyry and the hydrothermal auriferous lodes, in response to the parental magma evolution (late magmatic or early hydrothermal fluids) and subsequent ore-forming events, respectively. Characterization of chemical compositions of these two types of tourmaline growth during progressive exsolution of magma and subsequent hydrothermal crystallization has provided new insights into magmatic hydrothermal evolution, and the related ore-forming process.

2. Geological Setting

The West Qinling Orogen (WQO) is the western segment of the Qinling Orogen, which is bounded by the Linxia-Wushan-Tianshui Fault and Shangdan suture zone to the north and by the A'nimaque-Mianlue suture zone to the south (Figure 1a). The Shangdan suture zone witnesses the middle Paleozoic northward subduction of the Shangdan ocean (proto-Tethyan ocean) crust and subsequent collision between the North Qinling belt and Qinling terrane [22–24]. The A'nimaque-Mianlue Suture zone recorded the late Paleozoic to early Mesozoic subduction of the paleo-Tethyan oceanic crust and subsequent collision between the Yangtze Block, the Songpan-Ganzi terrane, and the Qinling terrane [25,26]. Lithologically, the WQO is dominated by a thick sequence of Paleozoic to early Mesozoic marine sedimentary rocks, with Archean to Proterozoic basement rocks exposed locally [23,24]. Brittle faults are well developed along several nearly E–W-trending fold and thrust belts in the WQO, and the thrust faults broadly coincide with the boundaries of major lithologic contacts [27]. Granitoid intrusions are widespread in the region. Available geochronological data indicate that most granitoid intrusions in the eastern part of the WQO were emplaced at 225–200 Ma [28,29], whereas the equivalents in the western part were mostly formed at 249–230 Ma [30,31], which has been interpreted to reflect a westward closure of the paleo-Tethyan ocean.

The Xiahe-Hezuo district is located in the western portion of the WQO (Figure 1a). It is dominated by weakly metamorphosed to unmetamorphosed Carboniferous to Middle Triassic marine sedimentary rocks [32], which were folded during the Triassic as outlined by the Xinpu-Lishishan anticline (Figure 1b). The district is divided into the western and eastern zones by the NW-striking Xiahe-Hezuo Fault. Secondary or higher order faults broadly parallel to the Xiahe-Hezuo Fault are well developed throughout the region (Figure 1b). Several Mesozoic granitoid plutons form a discontinuous NW-trending magmatic belt in the eastern zone, whereas numerous mafic to intermediate dikes are emplaced in the western zone. Some andesitic to dacitic volcanic rocks also outcrop sporadically (Figure 1b). Zircon U-Pb geochronology indicates that these igneous rocks emplaced and/or erupted between 252 and 233 Ma [30,31,33,34]. Combining the geology and geochemistry data, previous studies suggest these igneous rocks have formed along an active continental margin associated with the paleo-Tethyan subduction [31,35], or in a post-collision setting [30,36].

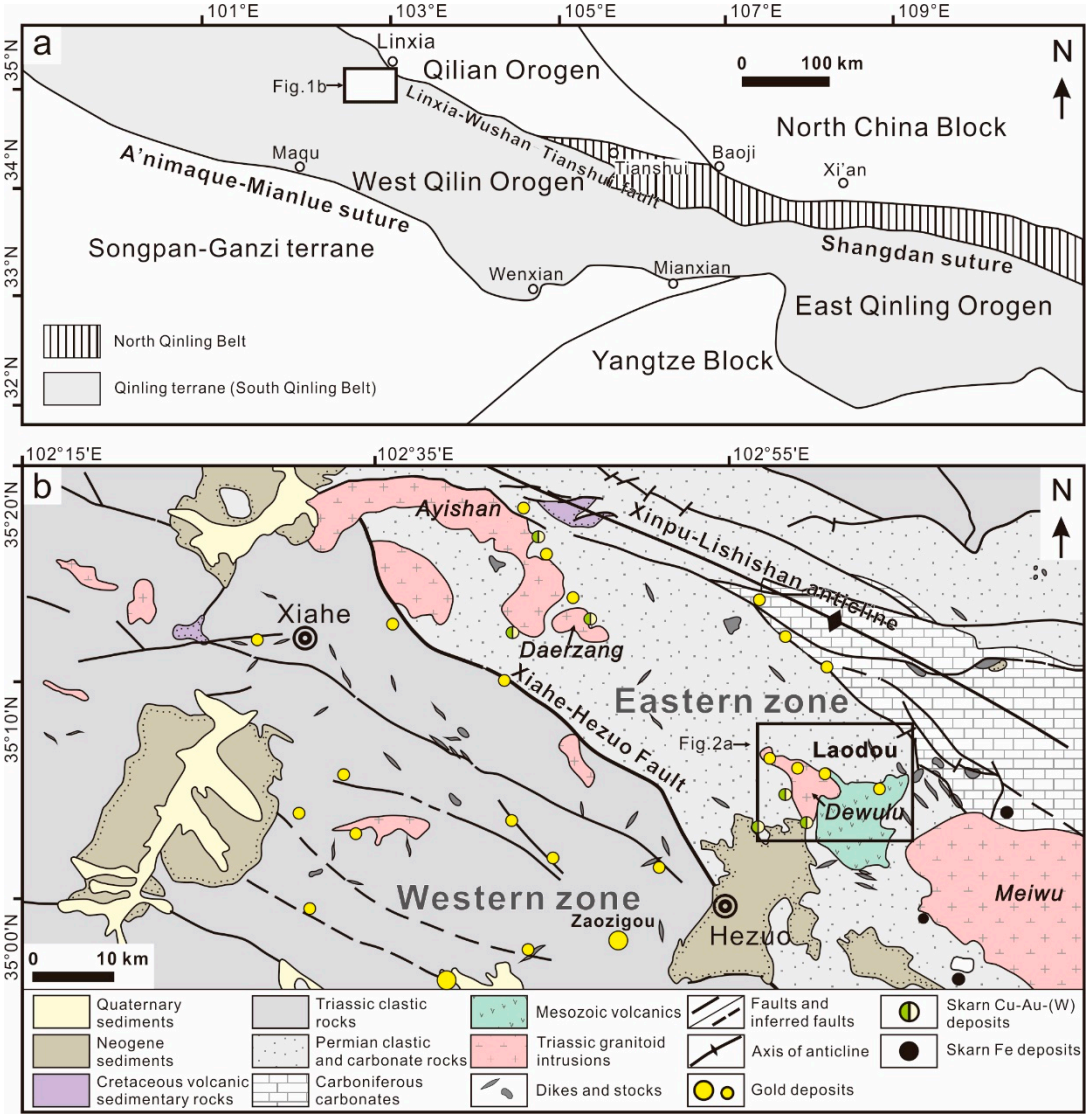

Figure 1. (**a**) Simplified map showing geotectonic terranes in the Qinling Orogen with the location of the study area [37,38]; (**b**) geologic map of the Xiahe-Hezuo district showing the distribution of major sedimentary facies, igneous rocks, and Au, Cu-Au-(W), and Fe deposits [39].

The Laodou gold deposit is a recently identified intrusion-related mineralization hosted in the quartz diorite porphyry of the Dewulu intrusive complex (Figure 2a). It has close spatial, temporal, and genetic relationships with igneous rocks, as well as the regional Cu-Au skarns and Au-Cu-As-W veins [33,37,39,40] (Figure 2a). The host quartz diorite porphyry consists of plagioclase, quartz, amphibole, and minor biotite. Zircon, apatite, and ilmenite are the main accessory minerals [31]. Tourmaline is locally abundant as disseminated crystals or tourmaline-quartz nodules. The magma origin has been interpreted as partial melting of K-rich meta-basaltic rocks in a thickened lower continental crust [31,41]. The deposit consists of five NNW- to N-striking auriferous lodes within the hydrothermally altered fault zones (F1–F5; Figure 2b). For example, the F1 altered fault zone contains five orebodies of Au2, Au2–1, Au8, Au8–1, and Au10, which strike at 286–354° and dip 27–38° to the east, and are 80–158 m long and 2.15–5.16 m thick, with a minimum vertical extent of 45–103 m (Figure 2c). The auriferous lode main includes quartz-sulfide-tourmaline and minor quartz-stibnite veins that are enveloped by potassic and phyllic alteration in the host quartz diorite porphyry (Figure 3). The mineral assemblages comprise mostly quartz, sericite, tourmaline, pyrite, arsenopyrite, and stibnite, with minor amounts of galena, sphalerite, chalcopyrite, tetrahedrite, and enargite. Gold occurs mainly

as "invisible gold" in pyrite (up to 66.65 ppm) and arsenopyrite (up to 4.32 ppm), and locally as submicrometer-sized particles of native gold [39,42]. The ore fluids are intermediate temperature (220–295 °C), low salinity (2–11 wt. % NaCl equiv), CO_2-rich, and moderately acidic to neutral aqueous fluids [42,43]. Stable isotopes of H-O-S-B-Pb supported a magmatic origin of the ore fluids, with minor external meteoric-derived groundwater also thought to be involved [39]. Two sericite samples—coeval with gold-bearing sulfides and native gold particles—yield indistinguishable plateau ages at 249 ± 1.5 Ma that, within analytical errors, agree with the zircon U-Pb age (247.6 ± 1.3 Ma) of the host quartz diorite porphyry [39].

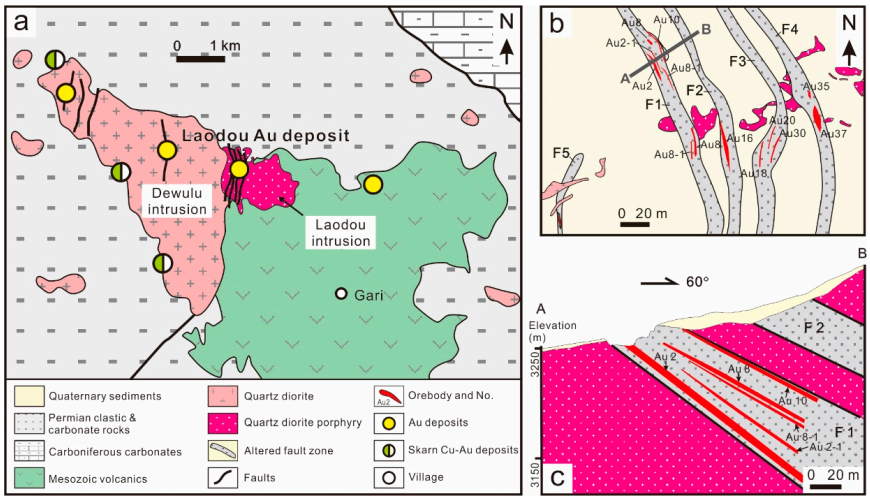

Figure 2. (**a**) Geologic map of the Dewulu intrusive complex with the location of the Laodou gold deposit. Other hydrothermal lode Au deposits and Cu-Au skarn deposits are also shown [44]; (**b**) simplified geologic map of the Laodou gold deposit; (**c**) representative cross section in (**b**) showing the geological relations between structures, alterations, and gold ores [39].

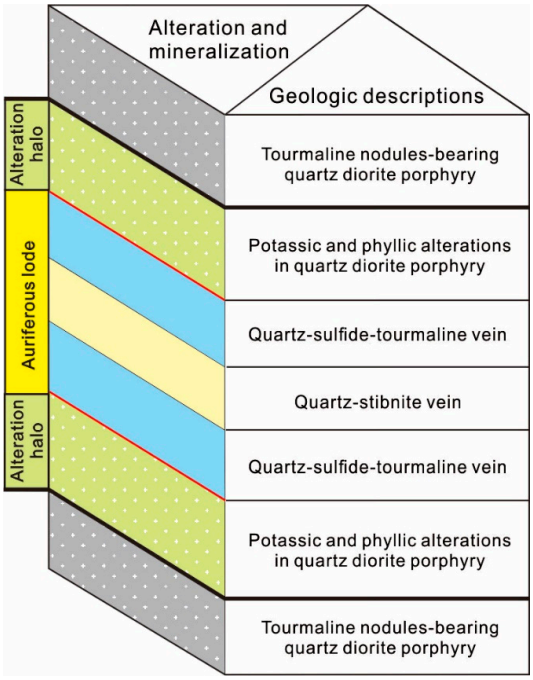

Figure 3. Idealized sketch of the auriferous lode that was enveloped by potassic and phyllic alteration in the host Laodou quartz diorite porphyry.

3. Tourmaline Occurrences

Tourmaline from the Laodou gold deposit is commonly black in field observations. According to the distinct occurrences and associated mineral assemblages, two types of tourmaline have been identified, including disseminated quartz-tourmaline nodules (type 1) in the host quartz diorite porphyry and quartz-sulfides-tourmaline veins (type 2) in the auriferous lodes.

3.1. Type 1 Tourmaline

Type 1 tourmaline is locally disseminated in the Laodou quartz diorite porphyry (Figure 4a) as quartz-tourmaline nodules that are usually several centimeters in diameter (Figure 4b). Some nodules display a leucocratic halo, which is mainly composed of fine-grained subhedral quartz and minor fine scaly sericite interstitial between quartz grains (Figure 4c). In most cases, quartz and tourmaline are intergrown and commonly characterized by a subhedral to anhedral granular texture, with straight or ragged boundaries (Figure 4d). In addition, some small tourmaline grains or fragments are wrapped by quartz that grew interstitially between the tourmaline grains (Figure 4d,e). The quartz-tourmaline nodules show a close spatial relationship with plagioclase, sericite, and muscovite (Figure 4e,f). Plagioclase is somewhat corroded, metasomatized, and then replaced by tourmaline (Figure 4e). Sericite and muscovite occur as fine scaly within the quartz-tourmaline nodules (Figure 4c), and remain the pseudomorph of plagioclase or biotite around the quartz-tourmaline nodules (Figure 4c,e,f).

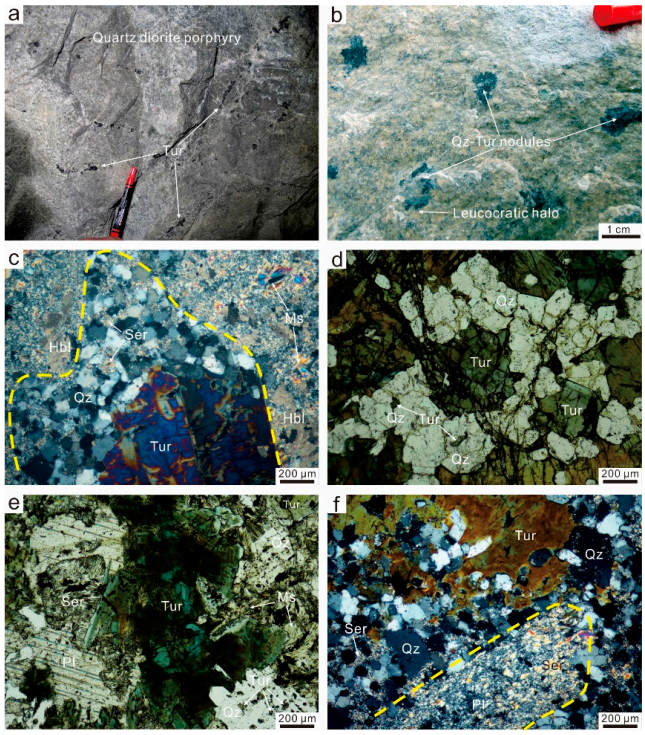

Figure 4. (**a**) Tourmaline occurs as disseminations in the quartz diorite porphyry; (**b**) quartz-tourmaline nodules in the quartz diorite porphyry display leucocratic haloes; (**c**) the leucocratic halo around a quartz-tourmaline nodule is mainly composed of fine-grained quartz and fine scaly sericite; (**d**) quartz and tourmaline in most nodules are intergrown and characterized by subhedral to anhedral granular textures with straight or ragged boundaries; (**e**) relationships between tourmaline, quartz, plagioclase, sericite, and muscovite; (**f**) sericite aggregates remain the pseudomorph of plagioclase or biotite around the quartz-tourmaline nodule. Tur—tourmaline; Qz—quartz; Hbl—hornblende; Ser—sericite; Pl—plagioclase; Ms—muscovite.

3.2. Type 2 Tourmaline

Type 2 tourmaline is represented by the open-space filling quartz-sulfide-tourmaline veins transecting the Laodou quartz diorite porphyry (Figure 5a), which are commonly several centimeters to half a meter wide with a variable length in auriferous lodes (Figure 2c). In this case, type 2 tourmaline is closely associated with arsenopyrite and commonly occurs either within the arsenopyrite vein (Figure 5a) or intergrown with the arsenopyrite disseminations (Figure 5b). Some fine-grained quartz-sulfide-tourmaline assemblages are present as the hydrothermal cement of breccias of altered quartz diorite porphyry (Figure 5c). Under microscope, type 2 tourmaline is characterized by an oscillatory-zoned texture of blue green to brown color, which has sharp, straight boundaries in contact with quartz and arsenopyrite (Figure 5d). In back scattered electron image, arsenopyrite exhibits either emulsion or hydrothermal filling textures in type 2 tourmaline (Figure 5e), implying they formed approximately at the same time. Other sulfides, including pyrite, tetrahedrite, and chalcopyrite, are generally interstitial between tourmaline grains (Figure 5f).

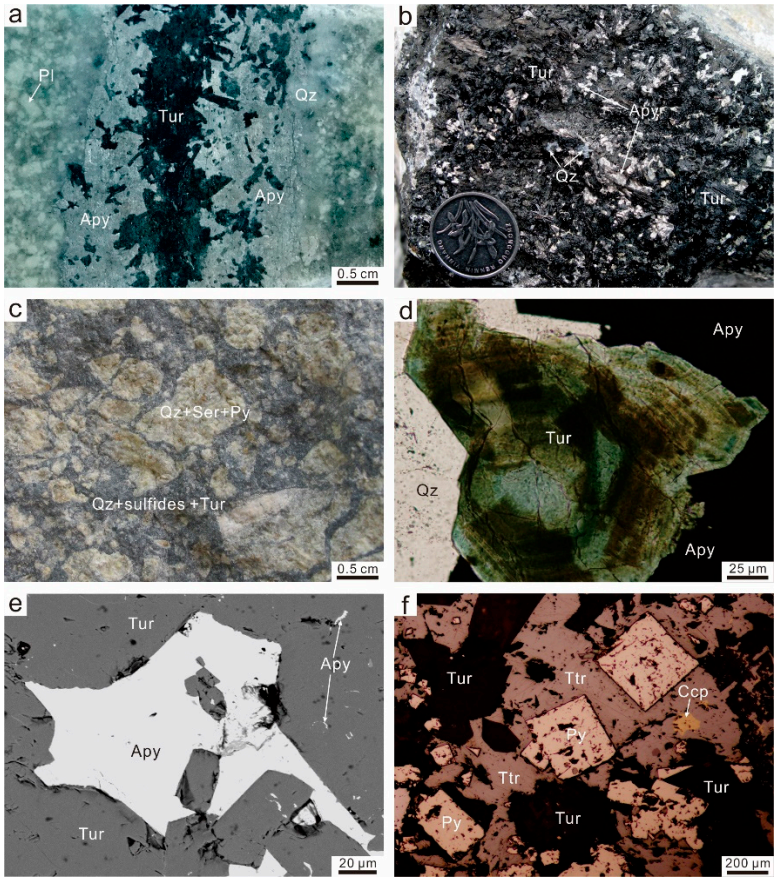

Figure 5. (**a**) Tourmaline occurs as quartz-sulfide-tourmaline veins transecting the quartz diorite porphyry; (**b**) tourmaline intergrown with arsenopyrite in a quartz-sulfide-tourmaline vein; (**c**) fine-grained quartz-sulfide-tourmaline cement the breccias of the altered quartz diorite porphyry; (**d**) tourmaline is characterized by an oscillatory-zoned texture of blue green to brown color, which has sharp, straight boundaries in contact with quartz and arsenopyrite; (**e**) arsenopyrite exhibits either emulsion or hydrothermal filling textures in type 2 tourmaline; (**f**) pyrite, tetrahedrite, and chalcopyrite are generally interstitial between tourmaline grains. Tur—tourmaline; Qz—quartz; Pl—plagioclase; Apy—arsenopyrite; Ser—sericite; Py—pyrite; Ttr—tetrahedrite; Ccp—chalcopyrite.

4. Sampling and Analytical Methods

Type 1 and type 2 tourmaline samples were collected from underground works and drill holes for this study. Double-polished thin sections of each type of tourmaline were examined under an optical microscope to reveal the paragenetic relationships and textural features.

4.1. Electron Microprobe Analysis

Back scattered electron (BSE) imaging and major element analysis using a JEOL JXA-8230 electron microprobe analyzer (EMPA) were completed at the Center for Global Tectonics, School of Earth Sciences, China University of Geosciences (Wuhan, China). The operating conditions were described in Wang et al. [45] and Ning et al. [46] in detail. We used the conditions of 15 kV accelerating voltage, 20 nA probe current, and a 1-micron beam diameter. The dwell times were 10 s on the element peaks and half that on the background locations adjacent to the peaks. Raw X-ray intensities were corrected using a ZAF (atomic number, absorption, fluorescence) correction procedure. A series of natural and synthetic SPI standards were utilized and changed based on the analyzing minerals. The following standards were used: andradite for Si and Ca, rutile for Ti, corundum for Al, hematite for Fe, rhodonite for Mn, pyrope garnet for Mg, albite for Na, sanidine for K, and apatite for P. We routinely analyzed two or three points from the core to rim of some large grains to check for chemical variations. The analyses were normalized to 15 cations (T + Z + Y) exclusive of Na, Ca, and K as suggested by Henry et al. [16]. All iron was assumed to be Fe^{2+}. The proportion of X site vacancies (□) was calculated as [1 − (Na + Ca + K)]. The B_2O_3 and H_2O contents were calculated from stoichiometric constraints assuming B = 3 atoms per formula unit (apfu) and OH^- = 3.5 apfu. Mineral formulae were calculated assuming 31 total anions (O^{2-} and OH^-).

4.2. Laser Ablation-ICPMS Analysis

Trace element analysis was conducted by LA-ICP-MS at the State Key Laboratory of Geological Processes and Mineral Resources (GPMR), China University of Geosciences (CUG), Wuhan, China. Detailed operating conditions for the laser ablation system and the ICP-MS instrument and data reduction have been previously described by Liu et al. [47]. Laser sampling was performed using a GeoLas 2005. An Agilent 7500a ICP-MS instrument was used to acquire ion-signal intensities, and the beam spot size was 44 μm. A "wire" signal smoothing device is included in this laser ablation system, by which smooth signals are produced even at very low laser repetition rates down to 1 Hz [48]. Helium was applied as a carrier gas. Argon was used as the make-up gas and mixed with the carrier gas via a T-connector before entering the ICP. Nitrogen was added into the central gas flow (Ar + He) of the Ar plasma to decrease the detection limit and improve precision [49]. Each analysis incorporated a background acquisition of approximately 20–30 s (gas blank) followed by 50 s of data acquisition from the sample. The Agilent Chemstation was utilized for the acquisition of each individual analysis. Element contents were calibrated against multiple-reference materials (BCR-2G, BIR-1G, BHVO-2G, and SRM610). Off-line selection and integration of background and analyte signals, and time-drift correction were performed by ICPMSDataCal [47], and quantitative calibration was undertaken using the method described by Chen et al. [50].

5. Results

5.1. Major Element Compositions

The major element compositions of type 1 and type 2 tourmaline samples from the Laodou gold deposit are listed in Table S1, and graphically shown in Figure 6. Type 1 tourmaline contains SiO_2 (33.6–35.1 wt.%), MgO (1.22–4.33 wt.%), Al_2O_3 (27.1–30.2 wt.%), FeO (14.6–19.8 wt.%), K_2O (0.034–0.056 wt.%), and MnO (0.16–0.31 wt.%). In contrast, type 2 tourmaline contains higher contents of SiO_2 (34.7–36.6 wt.%), MgO (5.69–9.72 wt.%), and Al_2O_3 (28.2–32.8 wt.%), and lower contents of FeO (5.79–13.5 wt.%), K_2O (0.015–0.032 wt.%), and MnO (0.013–0.028 wt.%) (Figure 6a–e).

Moreover, type 1 tourmaline shows narrow variations in CaO (0.97–1.66 wt.%), P_2O_5 (0.013–0.018 wt.%), and Na_2O (1.74–2.05 wt.%), while large variations in CaO (0.61–2.11 wt.%), P_2O_5 (0–0.023 wt.%), and Na_2O (1.49–2.23 wt.%) are observed in type 2 tourmaline (Figure 6f–h).

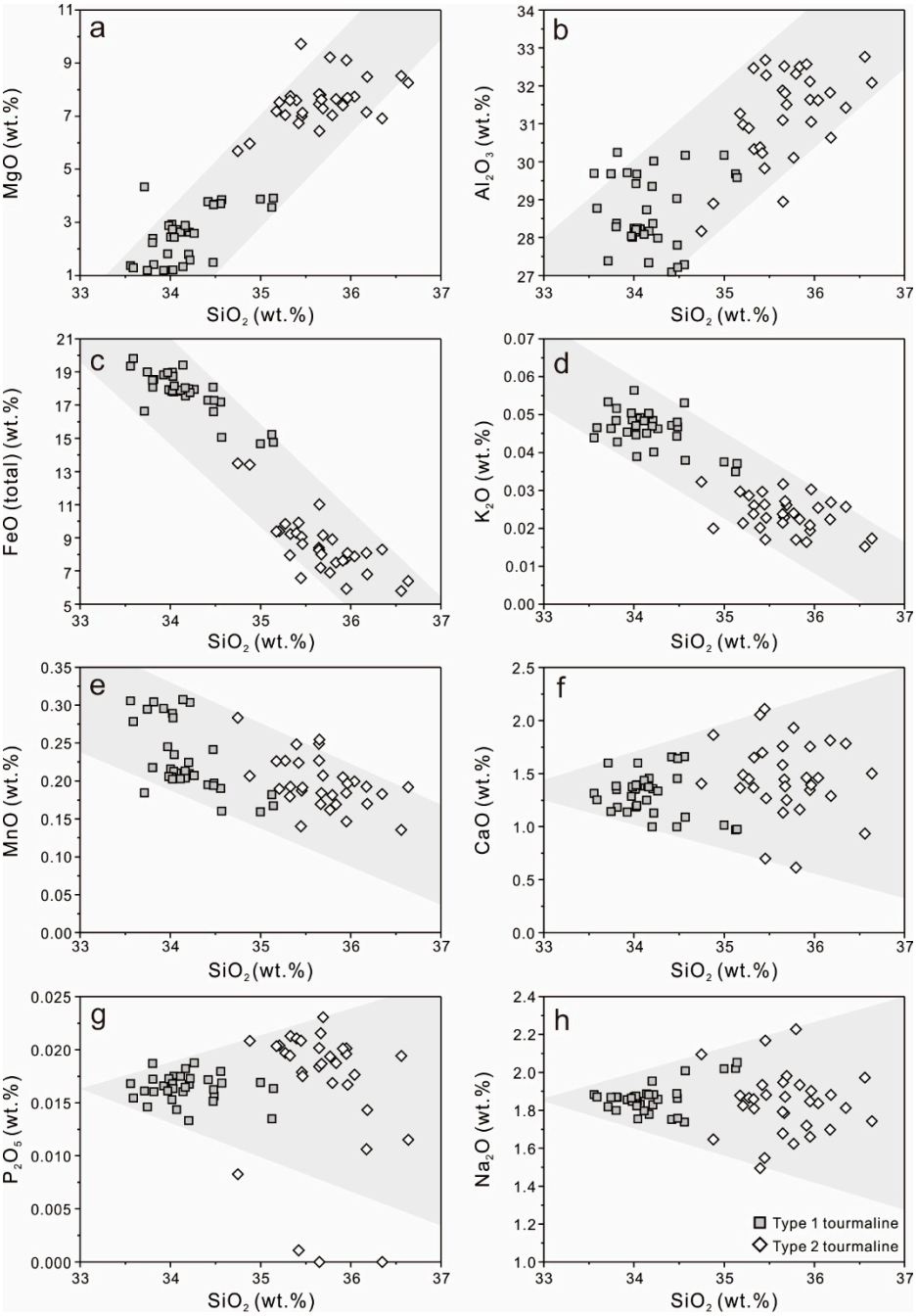

Figure 6. Major element variation diagrams for tourmaline from the Laodou gold deposit, showing the compositional differences between type 1 and type 2 tourmaline. (**a**) SiO_2 versus MgO; (**b**) SiO_2 versus Al_2O_3; (**c**) SiO_2 versus FeO (total); (**d**) SiO_2 versus K_2O; (**e**) SiO_2 versus MnO; (**f**) SiO_2 versus CaO; (**g**) SiO_2 versus P_2O_5; (**h**) SiO_2 versus Na_2O.

Both type 1 and type 2 tourmalines are classified in the alkali group based on the X-site occupancy [51] (Figure 7a). Type 1 tourmaline samples belong to schorl, with higher Fe/(Fe + Mg) ratios (0.68–0.90) and a narrow range of Na/(Na + Ca) ratios (0.65–0.79), whereas most type 2 tourmaline samples are dravite, with lower Fe/(Fe + Mg) ratios (0.27–0.57) and a larger range of Na/(Na + Ca) ratios

(0.57–0.87) [52] (Figure 7b). According to the ternary Al-Fe-Mg and Ca-Fe-Mg diagrams [53], both types of tourmaline are Al-rich and Ca-poor. Type 1 tourmaline has high Fe concentrations and plots in the fields of Li-poor granitoids and associated pegmatites and aplites, Fe^{3+}-rich quartz-tourmaline rocks (hydrothermally altered granites), and near Li-rich granitoids and associated pegmatites and aplites, whereas type 2 tourmaline contains high Mg and plots in the fields of metapelites and metapsammites not coexisting with an Al-saturating phase, Fe^{3+}-rich quartz-tourmaline rocks, calc silicate rocks, and metapelites, and Ca-poor metapelites, metapsammites, and quartz-tourmaline rocks (Figure 7c,d).

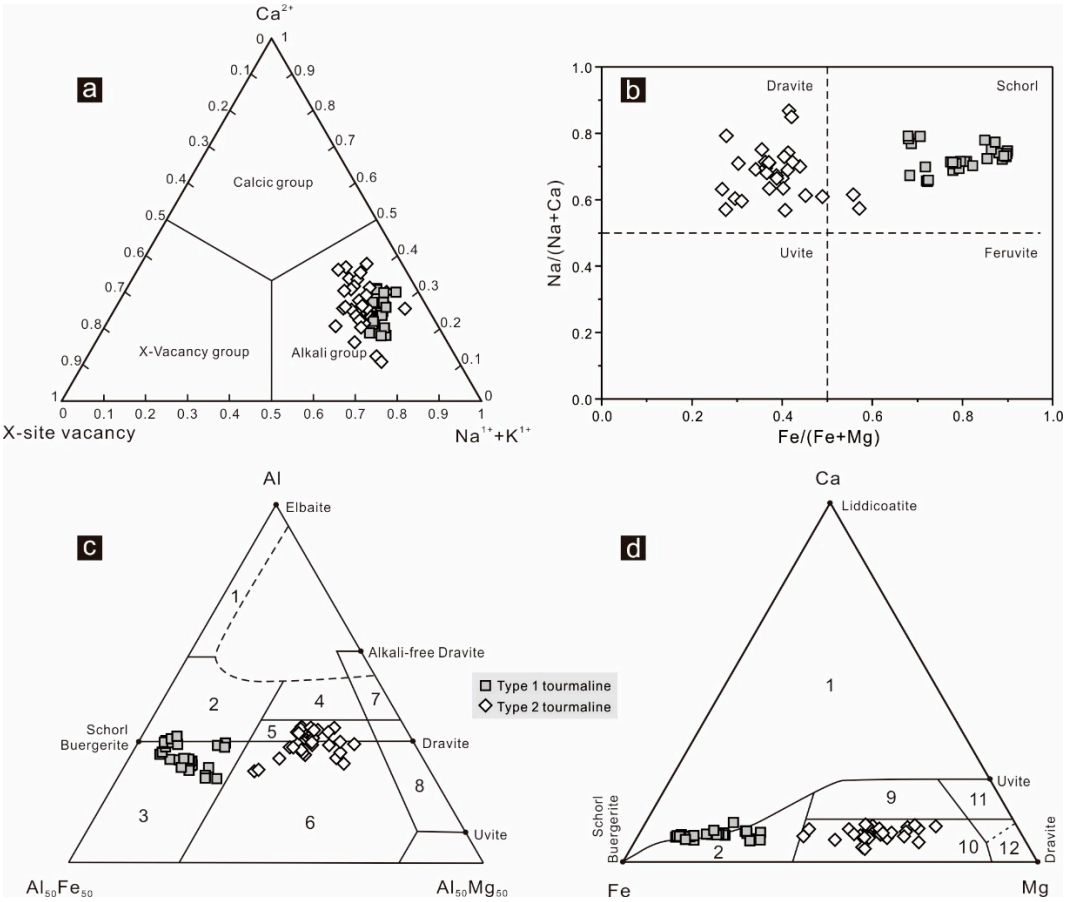

Figure 7. (**a**) Classification of the principal groups of tourmaline based on X-site occupancy [51]; (**b**) nomenclature of the tourmaline based on the classification diagram of Fe/(Fe + Mg) versus Na/(Na + Ca) [52]; (**c**,**d**) ternary Al-Fe-Mg and Ca-Fe-Mg diagrams showing compositions of tourmaline [53]. The regions define the compositions of tourmaline from different rock types. 1. Li-rich granitoids and associated pegmatites and aplites; 2. Li-poor granitoids and associated pegmatites and aplites; 3. Fe^{3+}-rich quartz-tourmaline rocks (hydrothermally altered granites); 4. Metapelites and metapsammites coexisting with an Al-saturating phase; 5. Metapelites and metapsammites not coexisting with an Al-saturating phase; 6. Fe^{3+}-rich quartz-tourmaline rocks, calc silicate rocks, and metapelites; 7. Low Ca metaultramafics and Cr, V-rich metasediments; 8. Metacarbonates and metapyroxenites; 9. Ca-rich metapelites, metapsammites, and calc-silicate rocks; 10. Ca-poor metapelites, metapsammites, and quartz-tourmaline rocks; 11. Metacarbonates; 12. Metaultramafics.

The binary diagrams show the compositional variation and substitution in type 1 and type 2 tourmaline samples. $FeMg_{-1}$ is suggested by the negative correlations between Fe and Mg in the two types of tourmaline samples (Figure 8a). However, the shift of the plots out of the northward arrow of $FeMg_{-1}$ suggest a substitution of Fe by Al (Figure 8b). This is proven by the strong negative correlation between Al and (Fe + Mg) (Figure 8c). The substitutions of $FeMg_{-1}$ and $FeAl_{-1}$ in type 1 and type 2 tourmaline are also supported by the projection of the data along the povondraite-"oxy-dravite" join,

because these plots fall roughly parallel to the $FeAl_{-1}$ and $AlO((Fe, Mg)(OH))_{-1}$ exchange vectors (Figure 8d). The positive correlation between X-site vacancy and Al suggests that the substitution of X-site vacancy Al_{-1} is also involved, alongside $FeMg_{-1}$, and $FeAl_{-1}$ in type 1 and type 2 tourmaline (Figure 8e). The Na content randomly distributes, along with the increase of X-site vacancy and Al, indicating that it is not the main influencing factor controlling the proportion of X-site vacancy and Al in tourmaline (Figure 8f,g). However, the negative correlation between X-site vacancy and Ca suggests that the X-site vacancy decrease in the tourmaline is caused by an increase of Ca content (Figure 8h), which suggests the substitution of X-site vacancy Ca_{-1} in type 1 and type 2 tourmaline.

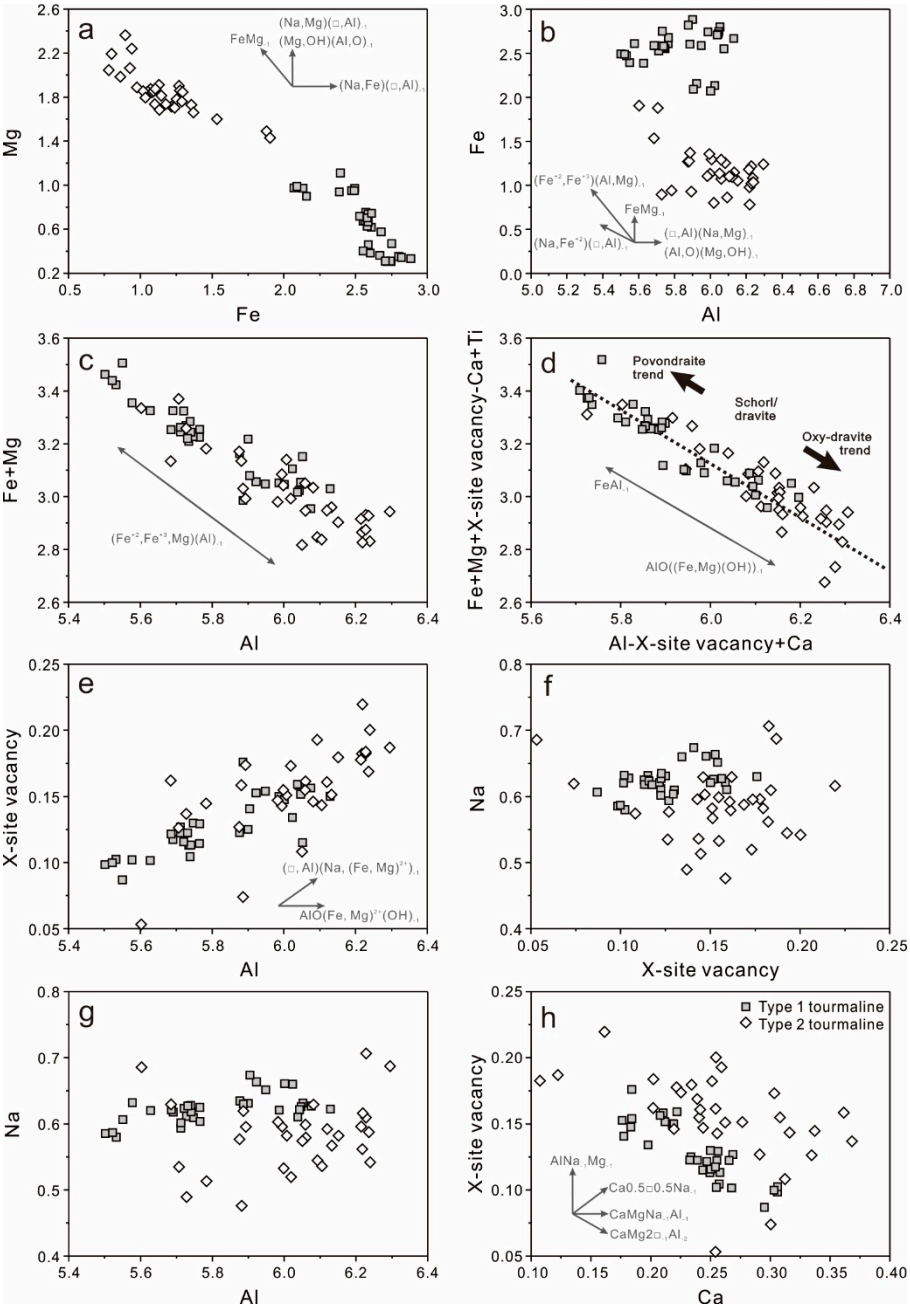

Figure 8. Binary composition diagrams of tourmaline expressed in terms atoms per formula unit (apfu). (**a**) Fe versus Mg; (**b**) Al versus Fe; (**c**) Al versus (Fe + Mg); (**d**) (Al-X-site vacancy + Ca) versus (Fe + Mg + X-site vacancy-Ca + Ti); (**e**) Al versus X-site vacancy; (**f**) X-site vacancy versus Na; (**g**) Ca versus X-site vacancy; (**h**) Al versus Na. Dominant substitution trends are indicated by arrows.

5.2. Trace and Rare Earth Element Compositions

The trace and rare earth element (REE) composition of type 1 and type 2 tourmaline samples from the Laodou gold deposit are summarized in Table S2 and plotted in Figures 9 and 10. Most trace element contents of type 1 and type 2 tourmaline vary between 0.1 and 10 ppm, except for some which are higher—up to hundreds of ppm in the cases of Sr, Sc, Sn, Cr, V, Mn, Zn, and Li, and some which are less than 0.1 ppm, such as Eu, Rb, Cs, Y, W, Bi, Th, and U (Table S2). Large ion lithophile elements (LILE) like Rb, Be, Ba, Cs, and K are relatively enriched in type 1 tourmaline compared to type 2 tourmaline, excluding Sr and Eu (Figure 9a). Most high field-strength elements (HFSEs), including Pb, Y, Sc, Nb, Ta, Ce, Hf, and REEs are also relatively enriched in type 1 tourmaline (Figure 9b). As for other elements, Sn, Cr, V, and Sb are enriched in type 2 tourmaline, whereas Mn, Zn, Li, Co, Cu, W, and Mo contents are higher in type 1 tourmaline (Figure 9c).

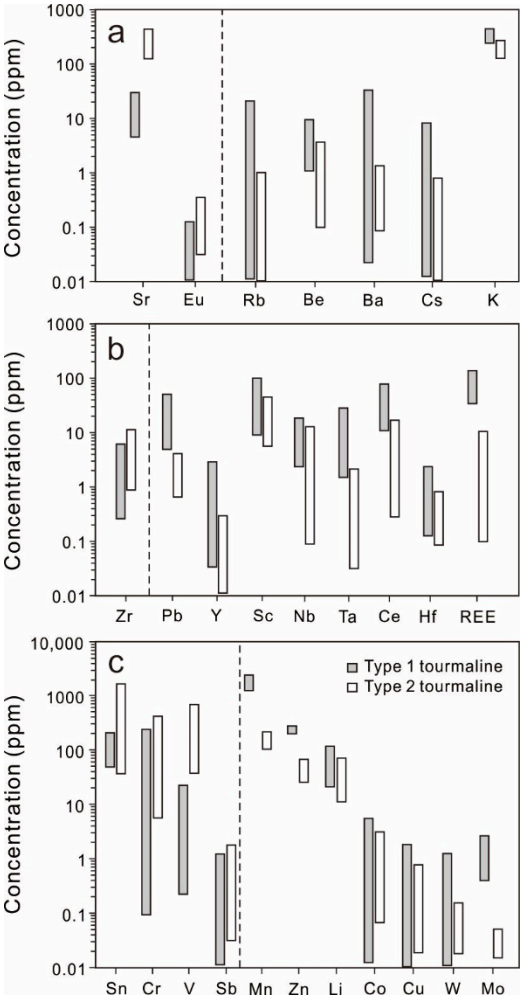

Figure 9. Concentration of (**a**) large ion lithophile elements (LILE); (**b**) high field-strength elements (HFSE); and (**c**) other trace elements in tourmaline from the Laodou gold deposit.

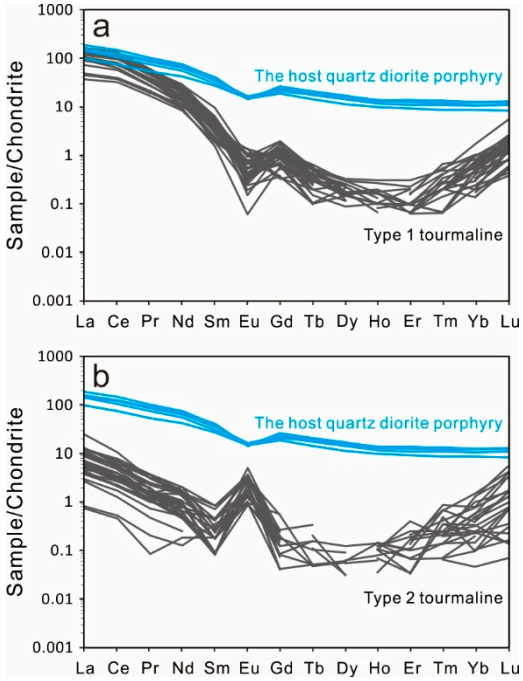

Figure 10. Chondrite-normalized [54] REE patterns of (**a**) type 1 tourmaline and (**b**) type 2 tourmaline from the Laodou gold deposit. Note that the chondrite-normalized REE patterns of the Laodou quartz diorite porphyry are also shown for comparison [31].

The REE concentrations and chondrite-normalized patterns of type 1 and type 2 tourmaline are different (Figure 10). As mentioned above, type 1 tourmaline contains higher REE concentrations than type 2 tourmaline (Figure 9b). Although both type 1 and type 2 tourmaline have similar asymmetric concave-upward shaped REE patterns with enrichment of LREE and HREE and depletion of MREE, type 1 tourmaline is characterized by a strong negative Eu anomaly (Eu* = 0–1.55; Figure 10a) whereas type 2 tourmaline has a strong positive Eu anomaly (Eu* = 2.33–40.15; Figure 10b). For comparison, the host quartz diorite porphyry has a similar asymmetric concave-upward shaped REE pattern, but typically has a higher REE concentration and relatively flat MREE and HREE patterns (Figure 10).

6. Discussion

6.1. Origin of Type 1 and Type 2 Tourmaline

Type 1 tourmaline occurs as disseminated quartz-tourmaline nodules in the Laodou quartz diorite porphyry. Quartz-tourmaline nodules in granite have been widely reported, and have been interpreted as (1) direct crystallization from a boron-rich granitic melt [55,56]; (2) magmatic-hydrothermal features related to the immiscible aqueous boron-rich fluids formed in the late stages of granite crystallization [20,57,58]; and (3) post-magmatic metasomatism by external boron-rich fluids through fractures [59]. Type 1 tourmaline occurs as inclusions in quartz, and grows interstitially between quartz grains (Figure 4d,e). This relationship suggests type 1 tourmaline and quartz formed at the same time. The presence of plagioclase replaced by tourmaline (Figure 4e) indicates that quartz-tourmaline nodules formed late in the crystallization sequence of the Laodou quartz diorite porphyry, rather than crystallizing directly from a boron-rich melt. The field observations showed that quartz-tourmaline nodules are texturally isolated aggregates dispersed in the quartz diorite porphyry without connections by any fractures (Figure 4b), indicating they are products of the crystallization of the quartz diorite porphyry and did not result from post-magmatic metasomatism by external boron-rich fluids infiltrating through fractures. Type 1 tourmaline samples are characterized by higher Fe and Al contents and lower Ca and Mg contents, and are mostly plotted in fields 2 and 3 of total Al-Fe-Mg and Ca-Fe-Mg

diagrams (Figure 7c,d), which is consistent with the fact that type 1 tourmaline is disseminated in the Laodou quartz diorite porphyry. Under the microscope, sericite and muscovite replacing plagioclase or biotite are distributed around the quartz-tourmaline nodules, reflecting the late internal infiltration of aqueous boron-rich fluids (Figure 4c,f). All these observations are consistent with the previous interpretation that quartz-tourmaline nodules formed from the magmatic hydrothermal fluids in the late crystallization sequence of the Laodou quartz diorite porphyry. This interpretation is also supported by the magmatic boron isotopic composition ($\delta^{11}B$ = –8.9–-5.5‰) of type 1 tourmaline [39].

Type 2 tourmaline occurs as radial crystal clusters in open-space filling quartz-sulfide-tourmaline veins (Figure 5a,b), indicating a hydrothermal origin. Type 2 tourmaline is commonly intergrown with arsenopyrite in the field, as shown by microscope observations (Figure 5). Mineral relations and textures, especially in the straight boundaries between arsenopyrite and tourmaline grains (Figure 5d) and the textures of arsenopyrite emulsion and/or infillings in tourmaline (Figure 5e), indicate the co-crystallization of type 2 tourmaline and arsenopyrite in the quartz-sulfide-tourmaline veins. Arsenopyrite is one of the gold-bearing sulfides in the Laodou deposit, containing detectable Au up to 4.32 ppm [42]. Thus, type 2 tourmaline, coexisting with Au-bearing arsenopyrite, can be interpreted as a hydrothermal product that crystallized from the ore-forming fluids of the Laodou gold deposit.

6.2. Records of Magmatic Hydrothermal Evolution

The composition of tourmaline is largely ruled by fluid/rock ratios and chemical equilibria with coexisting phases in the hydrothermal system [19]. In the Laodou deposit, type 1 tourmaline occurs as isolated quartz-tourmaline nodules in the quartz diorite porphyry, without connections by any fractures (Figure 4b), whereas type 2 tourmaline is represented as quartz-sulfide-tourmaline veins transecting the quartz diorite porphyry (Figures 2b and 5a). These field observations imply that type 1 tourmaline likely formed in a closed "rock-buffered" system with low fluid/rock ratios, whereas type 2 tourmaline crystallized in an open "fluid-buffered" system with high fluid/rock ratios. This interpretation is further supported by an oscillatory-zoned texture that is rare in type 1 tourmaline (Figure 4d) but is well-developed in type 2 tourmaline (Figure 5d), because the oscillatory zoning texture is commonly proposed as a record of high fluid/rock ratios in an open system [60]. Thus, type 1 tourmaline's chemistry is mainly controlled by the host quartz diorite porphyry, whereas type 2 tourmaline's chemistry retains some signatures of the ore-forming fluids. This is evidenced by the REE concentrations and REE patterns of type 1 and type 2 tourmaline, as discussed below.

Compared with the host quartz diorite porphyry, type 1 tourmaline has lower REE concentrations and a similar REE pattern, with a more negative Eu anomaly and higher contents of HREE. The lower REE concentrations in type 1 tourmaline are due to the co-crystallization of REE-rich apatite and zircon in the quartz diorite porphyry [20,31]. The similar REE patterns between type 1 tourmaline and the quartz diorite porphyry is the manifestation of the "source-inherited" characteristic. Tourmaline prefers Eu^{2+} over Eu^{3+}, but Eu^{3+} predominates in the magmatic melt [61]. This may explain type 1 tourmaline displaying a more negative Eu anomaly when crystallized from the low Eu^{2+} magmatic fluids generated by the exsolution of magmatic melt. The higher enrichment of HREE in type 1 tourmaline is mainly caused by the metasomatized and replaced plagioclase around the quartz-tourmaline nodules (Figure 4e,f), because HREE can be released from plagioclase more readily than Eu and LREE [62]. Likewise, this can also explain the enriched HREE in type 2 tourmaline, because quartz-sulfide-tourmaline veins are commonly enveloped by phyllic alteration (Figure 5a), reflecting the infiltration metasomatism represented by the formation of sericite as an alteration product of plagioclase [39]. Although type 2 tourmaline shows an asymmetric concave-upward REE pattern resembling type 1 tourmaline and the host quartz diorite porphyry, lower REE concentrations, and a strong positive Eu anomaly are exhibited (Figure 10b). Similar REE patterns are likely inherited from the magmatic fluids generated by the magma exsolution, which was evidenced by the below Co/Ni ratio constraints on the fluid provenance. The lower REE concentrations are likely caused by

the infiltration and dilution of the late inflow of meteoric fluids, characterized by low REE contents, which was supported by the reported H-O-B isotopic data of type 2 tourmaline [39]. The positive Eu anomaly of type 2 tourmaline does not reflect unusual redox conditions [7], except for the dominance of soluble Eu^{2+} over Eu^{3+} in fluids at temperature exceeding 200–250 °C [63]. This minimum temperature constraint is consistent with the microthermometry results of fluid inclusions (220–295 °C) in quartz from the quartz-sulfide-tourmaline veins [42,43].

6.3. Constraints on the Fluid Provenance

Previous studies have demonstrated that Co and Ni can partition strongly into tourmaline and arsenopyrite when they crystallize from ore-forming fluids [64,65]. In some cases, the Co/Ni ratio can be used as an index to place constraints on the source of ore-forming fluids [7,66]. In this study, type 2 tourmaline coexists with Au-bearing arsenopyrite in the auriferous lodes (Figure 5). It has been supposed that the Co/Ni ratios of coexisting arsenopyrite and tourmaline should represent the Co/Ni ratio of ore-forming fluids if they define a statistically significant linear trend [66]. The plotted Co and Ni contents of the coexisting type 2 tourmaline and arsenopyrite define a regression line with a squared correlation coefficient of 0.93 and an angular coefficient of 0.66 (Figure 11a). A correlation coefficient near 1 reflects the systematic tendency of Co and Ni to partition into tourmaline and arsenopyrite. The angular coefficient of 0.66 represents the Co/Ni ratio of the fluid from which the arsenopyrite and tourmaline precipitated. This value is close to the average Co/Ni ratio (0.43) of the Laodou quartz diorite porphyry [31]. We then plotted the Co and Ni contents of the Laodou quartz diorite porphyry for comparison. It is noted that these plots are comparable and restricted to the regression line that was defined by coexisting type 2 tourmaline and arsenopyrite (Figure 11a). The consistency of the projection data suggests that the related ore-forming fluids have a magmatic origin. This interpretation is further supported by the magmatic H-O-B isotopic signatures of type 2 tourmaline [39].

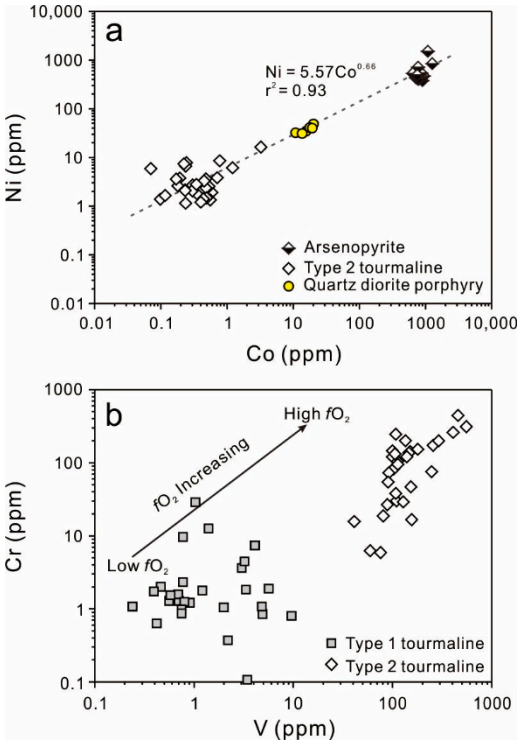

Figure 11. (**a**) Scatterplot of Co (ppm) versus Ni (ppm) in coexisting type 2 tourmaline and arsenopyrite [42] from the Laodou gold deposit. The Co and Ni contents of the host quartz diorite porphyry are shown for comparison [31]; (**b**) V (ppm) versus Cr (ppm) for type 1 and type 2 tourmaline samples from the Laodou gold deposit.

6.4. Redox State and Implications for Gold Precipitation

The ferric/ferrous ratios in tourmaline can be used as a monitor for changes in the redox state of hydrothermal fluids [19]. For example, it has been concluded that tourmaline in some porphyry Cu ± Mo deposits formed from oxidizing fluids based on their Al-poor composition and inverse Al-Fe correlations [67]. In this study, type 1 and type 2 tourmaline element plots showed a positive correlation between [Fe + Mg + X-site vacancy-Ca + Ti] and [Al-X-site + Ca], consistent with some involvement of the $FeAl_{-1}$ and/or $[AlO][(Fe, Mg)(OH)]_{-1}$ exchange vectors (Figure 8d). The compositions of tourmaline plots along the "oxy-dravite"–povondraite trend have been widely recognized in various hydrothermal systems [12,68]. This trend enables us to evaluate the significant proportion of the substitution of Al^{3+} by Fe^{3+}, and in turn implies changes of the redox state during tourmaline growth. Although there is some overlap of the type 1 and type 2 tourmaline points in the plot, type 1 tourmaline approaches the end member of povondraite, whereas type 2 tourmaline is plotted near the end member of oxy-dravite (Figure 8d). Accordingly, these plots show that more $[AlO][(Fe, Mg)(OH)]_{-1}$ is exchanged in type 2 tourmaline, and imply a more oxidizing environment for the formation of type 2 tourmaline.

The mobility of redox-sensitive trace elements is controlled by the changes of the redox state [69]. V and Cr are redox-sensitive elements and their concentrations in tourmaline are indicators of oxygen fugacity of the parental hydrothermal fluids [66]. This is because V is commonly transported in hydrothermal fluids as the soluble species V^{4+} and V^{5+}, rather than V^{3+} [70], whereas Cr is typically mobilized as Cr^{4+} under sufficiently oxidizing conditions [66]. Thus, the V and Cr concentrations in tourmaline have potential to act as an indicator of the redox state of hydrothermal fluids. In this study, type 2 tourmaline is characterized by remarkably higher V and Cr concentrations than type 1 tourmaline (Figure 11b), suggesting a higher oxygen fugacity of the parental fluids of type 1 tourmaline than type 2 tourmaline.

As mentioned above, type 2 tourmaline coexists with Au-bearing arsenopyrite in the auriferous lodes. Hence, the elevated concentrations of Fe^{3+}, V, and Cr in type 2 tourmaline fingerprint the increase of oxygen fugacity in the ore-forming fluids. This is consistent with the H-O-B isotopic data of type 2 tourmaline, which indicate the input of external meteoric-derived groundwater during precipitation of the quartz-sulfide-tourmaline veins [39]. The related fluid mixing would most likely lead to the increase of oxygen fugacity in the ore-forming fluids. In addition, gold as bisulfide ($Au(HS)_2^-$) complexes is widely acknowledged to account for gold transport in acidic reducing ore fluids in meso-epithermal ore-forming systems [71]. Increasing oxygen fugacity will destabilize $Au(HS)_2^-$ [72], facilitating the precipitation of gold in arsenopyrite and/or arsenian pyrite, and/or as native gold. Thus, we propose that the most important consequence of the increase of oxygen fugacity in the ore-forming fluids is acting as a trigger response for the precipitation of gold.

7. Conclusions

(1) Two types of tourmaline are recognized in the Laodou deposit. Type 1 tourmaline occurs as quartz-tourmaline nodules within the quartz diorite porphyry, whereas type 2 tourmaline occurs as quartz-sulfide-tourmaline veins in auriferous lodes.

(2) Both tourmaline types fall into the alkali group and are classified under the schorl-dravite solid solution series. The substitutions of $FeMg_{-1}$, $FeAl_{-1}$, $AlO((Fe, Mg)(OH))_{-1}$, and X-site vacancy Ca_{-1} are inferred by the variations of their major element compositions.

(3) Type 1 tourmaline samples are magmatic tourmaline, and were produced by the late crystallization process of the quartz diorite porphyry; type 2 tourmaline samples coexist with Au-bearing arsenopyrite and are crystallized from ore-forming fluids. Their REE compositions record the related magmatic-hydrothermal evolution.

(4) The Co/Ni ratios of the coexisting type 2 tourmaline and arsenopyrite are close to that of the host quartz diorite porphyry, indicating a magma origin of the ore-forming fluids.

(5) The elevated concentrations of Fe^{3+}, V, and Cr in type 2 tourmaline fingerprint the increase of the oxygen fugacity in the ore-forming fluids, which is a trigger of gold precipitation.

Supplementary Materials: The following are available online at http://www.mdpi.com/2075-163X/10/8/647/s1, Table S1: Major element compositions of type 1 and type 2 tourmaline samples from the Laodou gold deposit, Table S2: Trace element compositions of type 1 and type 2 tourmaline samples from the Laodou gold deposit.

Author Contributions: Conceptualization, X.J. and J.S.; investigation, X.J. and J.S.; data curation, X.J.; writing—original draft preparation, X.J.; writing—review and editing, X.J. and J.S. All authors have read and agreed to the published version of the manuscript.

Funding: This research was funded by the National Natural Science Foundation of China (Grant No. 41772081, 41072057).

Acknowledgments: We are grateful to Chenzhou Mining Limited for access to the mine and to Liangping Dong for geologic guidance. We also gratefully acknowledgment Zhaochu Hu, Jie Lin, and Chunfei Chen for their help with LA-ICPMS analysis.

Conflicts of Interest: The authors declare no conflict of interest.

References

1. Williamson, B.J.; Spratt, J.; Adams, J.T.; Tindle, A.G.; Stanley, C.J. Geochemical constraints from zoned hydrothermal tourmalines on fluid evolution and Sn mineralization: An example from fault breccias at Roche, SW England. *J. Petrol.* **2000**, *41*, 1439–1453. [CrossRef]
2. Sushchevskaya, T.; Ignatiev, A.; Velivetskaya, T. Magmatic Nature of Mineralizing Fluids in the Solnechnoye Sn Deposit (Russia) Deduced from Isotopic (H, O) Compositions of Tourmaline. *Resour. Geol.* **2011**, *61*, 407–413. [CrossRef]
3. Codeço, M.S.; Weis, P.; Trumbull, R.B.; Pinto, F.; Lecumberri-Sanchez, P.; Wilke, F.D.H. Chemical and boron isotopic composition of hydrothermal tourmaline from the Panasqueira W-Sn-Cu deposit, Portugal. *Chem. Geol.* **2017**, *468*, 1–16. [CrossRef]
4. Yavuz, F.; Iskenderoglu, A.; Jiang, S.Y. Tourmaline compositions from the Salikvan porphyry Cu-Mo deposit and vicinity, northeastern Turkey. *Can. Mineral.* **1999**, *37*, 1007–1023.
5. Dill, H.G.; Garrido, M.M.; Melcher, F.; Gomez, M.C.; Luna, L.I. Depth-related variation of tourmaline in the breccia pipe of the San Jorge porphyry copper deposit, Mendoza, Argentina. *Ore Geol. Rev.* **2012**, *48*, 271–277. [CrossRef]
6. Garda, G.M.; Trumbull, R.B.; Beljavskis, P.; Wiedenbeck, M. Boron isotope composition of tourmalinite and vein tourmalines associated with gold mineralization, Serra do Itaberaba Group, central Ribeira Belt, SE Brazil. *Chem. Geol.* **2009**, *264*, 207–220. [CrossRef]
7. Trumbull, R.B.; Garda, G.M.; Xavier, R.P.; Cavalcanti, J.A.D.; Codeço, M.S. Tourmaline in the Passagem de Mariana gold deposit (Brazil) revisited: Major-element, trace-element and B-isotope constraints on metallogenesis. *Miner. Depos.* **2019**, *54*, 395–414. [CrossRef]
8. Daver, L.; Jébrak, M.; Beaudoin, G.; Trumbull, R.B. Three-stage formation of greenstone-hosted orogenic gold deposits in the Val-d'Or mining district, Abitibi, Canada: Evidence from pyrite and tourmaline. *Ore Geol. Rev.* **2020**, *120*, 103449. [CrossRef]
9. Slack, J.F.; Palmer, M.R.; Stevens, B.P.J.; Barnes, R.G. Origin and significance of tourmaline-rich rocks in the Broken Hill district, Australia. *Econ. Geol.* **1993**, *88*, 505–541. [CrossRef]
10. Griffin, W.L.; Slack, J.F.; Ramsden, A.R.; Win, T.T.; Ryan, C.G. Trace elements in tourmalines from massive sulfides deposits and tourmalinites; geochemical controls and exploration applications. *Econ. Geol.* **1996**, *91*, 657–675. [CrossRef]
11. Jiang, S.Y.; Palmer, M.R.; Slack, J.F.; Shaw, D.R. Boron isotope systematics of tourmaline formation in the Sullivan Pb–Zn–Ag deposit, British Columbia, Canada. *Chem. Geol.* **1999**, *158*, 131–144. [CrossRef]
12. Tornos, F.; Wiedenbeck, M.; Velasco, F. The boron isotope geochemistry of tourmaline-rich alteration in the IOCG systems of northern Chile: Implications for a magmatic-hydrothermal origin. *Miner. Depos.* **2011**, *47*, 483–499. [CrossRef]

13. Xavier, R.P.; Wiedenbeck, M.; Trumbull, R.B.; Dreher, A.M.; Monteiro, L.V.S.; Rhede, D.; De Araujo, C.E.G.; Torresi, I. Tourmaline B-isotopes fingerprint marine evaporites as the source of high-salinity ore fluids in iron oxide copper-gold deposits, Carajás Mineral Province (Brazil). *Geology* **2008**, *36*, 743–746. [CrossRef]
14. Kelly, C.J.; Davis, W.J.; Potter, E.G.; Corriveau, L. Geochemistry of hydrothermal tourmaline from IOCG occurrences in the Great Bear magmatic zone: Implications for fluid source(s) and fluid composition evolution. *Ore Geol. Rev.* **2020**, *118*, 103329. [CrossRef]
15. Dutrow, B.L.; Henry, D.J. Tourmaline: A geologic DVD. *Elements* **2011**, *7*, 301–306. [CrossRef]
16. Henry, D.J.; Novák, M.; Hawthorne, F.C.; Ertl, A.; Dutrow, B.L.; Uher, P.; Pezzotta, F. Nomenclature of the tourmaline-supergroup minerals. *Am. Miner.* **2011**, *96*, 895–913. [CrossRef]
17. van Hinsberg, V.J.; Henry, D.J.; Dutrow, B.L. Tourmaline as a petrologic forensic mineral: A unique recorder of its geologic past. *Elements* **2011**, *7*, 327–332. [CrossRef]
18. Dutrow, B.L.; Henry, D.J. Tourmaline compositions and textures: Reflections of the fluid phase. *J. Geosci.* **2018**, *63*, 99–110. [CrossRef]
19. Slack, J.F.; Trumbull, R.B. Tourmaline as a recorder of ore-forming processes. *Elements* **2011**, *7*, 321–326. [CrossRef]
20. Yang, S.Y.; Jiang, S.Y.; Zhao, K.D.; Dai, B.Z.; Yang, T. Tourmaline as a recorder of magmatic–hydrothermal evolution: An in situ major and trace element analysis of tourmaline from the Qitianling batholith, South China. *Contrib. Mineral. Petrol.* **2015**, *170*, 1–21. [CrossRef]
21. Hu, D.L.; Jiang, S.Y. In-situ elemental and boron isotopic variations of tourmaline from the Maogongdong deposit in the Dahutang W-Cu ore field of northern Jiangxi Province, South China: Insights into magmatic-hydrothermal evolution. *Ore Geol. Rev.* **2020**, *122*, 103502. [CrossRef]
22. Kröner, A.; Zhang, G.W.; Sun, Y. Granulites in the Tongbai area, Qinling belt, China: Geochemistry, petrology, single zircon geochronology, and implications for the tectonic evolution of eastern Asia. *Tectonics* **1993**, *12*, 245–255. [CrossRef]
23. Zhang, G.W. *Qinling Orogenic Belt and Continental Dynamics*; Science Press: Beijing, China, 2001; 855p. (In Chinese)
24. Dong, Y.P.; Zhang, G.W.; Neubauer, F.; Liu, X.M.; Genser, J.; Hauzenberger, C. Tectonic evolution of the Qinling orogen, China: Review and synthesis. *J. Asian Earth Sci.* **2011**, *41*, 213–237. [CrossRef]
25. Meng, Q.R.; Zhang, G.W. Geologic framework and tectonic evolution of the Qinling orogen, central China. *Tectonophysics* **2000**, *323*, 183–196. [CrossRef]
26. Zhang, G.W.; Guo, A.L.; Yao, A.P. Western Qinling—Songpan continental tectonic node in China's continental tectonics. *Earth Sci. Front.* **2004**, *11*, 23–32, (In Chinese with English Abstract).
27. Zhu, L.M.; Zhang, G.W.; Yang, T.; Wang, F.; Gong, H.J. Geochronology, petrogenesis and tectonic implications of the Zhongchuan granitic pluton in the Western Qinling metallogenic belt, China. *Geol. J.* **2013**, *48*, 310–334. [CrossRef]
28. Sun, W.D.; Li, S.G.; Chen, Y.D.; Li, Y.J. Timing of synorogenic granitoids in the South Qinling, central China: Constraints on the evolution of the Qinling-Dabie Orogenic belt. *J. Geol.* **2002**, *110*, 457–468. [CrossRef]
29. Qin, J.F.; Lai, S.C.; Grapes, R.; Diwu, C.R.; Ju, Y.J.; Li, Y.F. Geochemical evidence for origin of magma mixing for the Triassic monzonitic granite and its enclaves at Mishuling in the Qinling orogen (central China). *Lithos* **2009**, *112*, 259–276. [CrossRef]
30. Luo, B.J.; Zhang, H.F.; Lü, X.B. U–Pb zircon dating, geochemical and Sr–Nd–Hf isotopic compositions of Early Indosinian intrusive rocks in West Qinling, central China: Petrogenesis and tectonic implications. *Contrib. Mineral. Petrol.* **2012**, *164*, 551–569. [CrossRef]
31. Jin, X.Y.; Li, J.W.; Sui, J.X.; Wen, G.; Zhang, J.Y. Geochronological and geochemical constraints on the genesis and tectonic setting of Dewulu intrusive complex in Xiahe-Hezuo district of Western Qinling Orogen. *J. Earth Sci. Environ.* **2013**, *35*, 20–38, (In Chinese with English Abstract).
32. Kou, X.H.; Zhang, K.X.; Lin, Q.X.; Zhu, Y.H.; Chen, F.N.; Luo, G.M.; Xu, Y.D. The distribution of Permian sedimentary sequences in the adjacent area of Qinling-Qilian-Kunlun, central China. *Earth Sci. J. China Univ. Geosci.* **2007**, *32*, 681–690, (In Chinese with English Abstract).
33. Sui, J.X.; Li, J.W.; Jin, X.Y.; Vasconcelos, P.; Zhu, R. $^{40}Ar/^{39}Ar$ and U-Pb constraints on the age of the Zaozigou gold deposit, Xiahe-Hezuo district, West Qinling orogen, China: Relation to early Triassic reduced intrusions emplaced during slab rollback. *Ore Geol. Rev.* **2018**, *101*, 885–899. [CrossRef]

34. Yu, H.C.; Qiu, K.F.; Nassif, M.T.; Geng, J.Z.; Sai, S.X.; Duo, D.W.; Huang, Y.Q.; Wang, J. Early orogenic gold mineralization event in the West Qinling related to closure of the Paleo-Tethys Ocean—Constraints from the Ludousou gold deposit, central China. *Ore Geol. Rev.* **2020**, *117*, 103217. [CrossRef]
35. Guo, X.Q.; Yan, Z.; Wang, Z.Q.; Wang, T.; Hou, K.J.; Fu, C.L.; Li, J.L. Middle Triassic arc magmatism along the northeastern margin of the Tibet: U-Pb and Lu-Hf zircon characterization of the Gangcha complex in the West Qinling terrane, central China. *J. Geol. Soc.* **2012**, *169*, 327–336. [CrossRef]
36. Zhang, C.L.; Wang, T.; Wang, X.X. Origin and tectonic setting of the early Mesozoic granitoids in Qinling orogenic belt, China. *Geol. J. China Univ.* **2008**, *14*, 304–316, (In Chinese with English Abstract).
37. Sui, J.X.; Li, J.W.; Hofstra, A.H.; Obrien, H.; Lahaye, Y.; Yan, D.R.; Li, Z.K.; Jin, X.Y. Genesis of the Zaozigou gold deposit, West Qinling orogen, China: Constraints from sulfide trace element and stable isotope geochemistry. *Ore Geol. Rev.* **2020**, *122*, 103477. [CrossRef]
38. Wang, J.P.; Liu, Z.J.; Liu, J.J.; Zeng, X.T.; Wang, K.X.; Liu, B.Z.; Wang, H.; Liu, C.H.; Zhang, F.F. Trace element compositions of pyrite from the Shuangwang gold breccias, Western Qinling Orogen, China: Implications for deep ore prediction. *J. Earth Sci.* **2018**, *29*, 564–572. [CrossRef]
39. Jin, X.Y.; Li, J.W.; Hofstra, A.H.; Sui, J.X. Magmatic-hydrothermal origin of the early Triassic Laodou lode gold deposit in the Xiahe-Hezuo district, West Qinling orogen, China: Implications for gold metallogeny. *Miner. Depos.* **2017**, *52*, 883–902. [CrossRef]
40. Sui, J.X.; Li, J.W.; Wen, G.; Jin, X.Y. The Dewulu Reduced Au-Cu skarn deposit in the Xiahe-Hezuo district, West Qinling orogen, China: Implications for an intrusion-related gold system. *Ore Geol. Rev.* **2016**, *80*, 1230–1244. [CrossRef]
41. Zhang, D.X.; Shu, Z.X.; Cao, H.; Lu, A.H. Indosinian magmatism and tectonic setting of Xiahe-Hezuo area, western Qinling Mountains—Implications from the Dewulu quartz diorite and Laodou quartz diorite porphyry. *Geol. China* **2015**, *42*, 1257–1273, (In Chinese with English Abstract).
42. Jin, X.Y. Genesis of the Laodou Gold Deposit, Xiahe-Hezuo Area, West Qinling Orogen: Constraints from the Geochemistry and Isotopic Geochronology. Master's Thesis, China University of Geosciences, Wuhan, China, 2013.
43. Wang, F. Discussion of the metallogenic geological conditions and ore genesis of the Laodou gold deposit in Gansu Province. *Gansu Metall.* **2004**, *26*, 16–18, (In Chinese with English Abstract).
44. Zhou, J.B. Study on geological characteristics and metallogenic mechanism of the Laodou gold deposit in Gansu province, China. *Gansu Metall.* **2011**, *33*, 56–60, (In Chinese with English Abstract).
45. Wang, J.P.; Li, X.W.; Ning, W.B.; Kusky, T.; Wang, L.; Polat, A.; Deng, H. Geology of a Neoarchean suture: Evidence from the Zunhua ophiolitic mélange of the Eastern Hebei Province, North China Craton. *GSA Bull.* **2019**, *131*, 1943–1964. [CrossRef]
46. Ning, W.B.; Wang, J.P.; Xiao, D.; Li, F.F.; Huang, B.; Fu, D. Electron probe microanalysis of monazite and its applications to U-Th-Pb dating of geological samples. *J. Earth Sci.* **2019**, *30*, 952–963. [CrossRef]
47. Liu, Y.S.; Hu, Z.C.; Gao, S.; Günther, D.; Xu, J.; Gao, C.G.; Chen, H.H. In situ analysis of major and trace elements of anhydrous minerals by LA-ICP-MS without applying an internal standard. *Chem. Geol.* **2008**, *257*, 34–43. [CrossRef]
48. Hu, Z.C.; Liu, Y.S.; Gao, S.; Xiao, S.Q.; Zhao, L.S.; Günther, D.; Li, M.; Zhang, W.; Zong, K.Q. A "wire" signal smoothing device for laser ablation inductively coupled plasma mass spectrometry analysis. *Spectrochim. Acta Part B At. Spectrosc.* **2012**, *78*, 50–57. [CrossRef]
49. Hu, Z.C.; Gao, S.; Liu, Y.S.; Hu, S.H.; Chen, H.H.; Yuan, H.L. Signal enhancement in laser ablation ICP-MS by addition of nitrogen in the central channel gas. *J. Anal. At. Spectrom.* **2008**, *23*, 1093–1101. [CrossRef]
50. Chen, C.F.; Liu, X.G.; Hu, Z.C.; Zong, K.Q.; Liu, Y.S. In situ analysis of the major and trace element compositions of hydrous silicate minerals by LA-ICP-MS. *Earth Sci. J. China Univ. Geosci.* **2014**, *39*, 525–536, (In Chinese with English Abstract).
51. Hawthorne, F.C.; Henry, D.J. Classification of the minerals of the tourmaline group. *Eur. J. Mineral.* **1999**, *11*, 201–216. [CrossRef]
52. Jiang, S.Y.; Palmer, M.R.; Yeats, C.J. Chemical and boron isotopic compositions of tourmaline from the Archean Big Bell and Mount Gibson gold deposits, Murchison Province, Yilgarn Craton, Western Australia. *Chem. Geol.* **2002**, *188*, 229–247. [CrossRef]
53. Henry, D.J.; Guidotti, C.V. Tourmaline as a petrogenetic indicator mineral- An example from the staurolite-grade metapelites of NW Maine. *Am. Mineral.* **1985**, *70*, 1–15.

54. Sun, S.S.; Mcdonough, W.F. Chemical and isotopic systematics of oceanic basalts: Implications for mantle composition and processes. *Geol. Soc. Lond. Spec. Publ.* **1989**, *42*, 313–345. [CrossRef]
55. Perugini, D.; Poli, G. Tourmaline nodules from Capo Bianco aplite (Elba Island, Italy): An example of diffusion limited aggregation growth in a magmatic system. *Contrib. Mineral. Petrol.* **2007**, *153*, 493–508. [CrossRef]
56. Longfellow, K.M.; Swanson, S.E. Skeletal tourmaline, undercooling, and crystallization history of the Stone Mountain granite, Georgia, USA. *Can. Mineral.* **2011**, *49*, 341–357. [CrossRef]
57. Samson, I.M.; Sinclair, W.D. Magmatic hydrothermal fluids and the origin of quartz-tourmaline orbicules in the Seagull Batholith, Yukon Territory. *Can. Mineral.* **1992**, *30*, 937–954.
58. Trumbull, R.B.; Krienitz, M.S.; Gottesmann, B.; Wiedenbeck, M. Chemical and boron-isotope variations in tourmalines from an S-type granite and its source rocks: The Erongo granite and tourmalinites in the Damara Belt, Namibia. *Contrib. Mineral. Petrol.* **2008**, *155*, 1–18. [CrossRef]
59. Rozendaal, A.; Bruwer, L. Tourmaline nodules: Indicators of hydrothermal alteration and Sn-Zn-(W) mineralization in the Cape Granite Suite, South Africa. *J. Afr. Earth Sci.* **1995**, *21*, 141–155. [CrossRef]
60. Taylor, B.E.; Slack, J.F. Tourmalines from Appalachian-Caledonian massive sulfide deposits; textural, chemical, and isotopic relationships. *Econ. Geol.* **1984**, *79*, 1703–1726. [CrossRef]
61. van Hinsberg, V.J. Preliminary experimental data on trace-element partitioning between tourmaline and silicate melt. *Can. Mineral.* **2011**, *49*, 153–163. [CrossRef]
62. Shibata, S.N.; Tanaka, T.; Yamamoto, K. Crystal structure control of the dissolution of rare earth elements in water-mineral interactions. *Geochem. J.* **2006**, *40*, 437–446. [CrossRef]
63. Bau, M.; Möller, P. Rare earth element fractionation in metamorphogenic hydrothermal calcite, magnesite and siderite. *Mineral. Petrol.* **1992**, *45*, 231–246. [CrossRef]
64. Klemme, S.; Marschall, H.R.; Jacob, D.E.; Prowatke, S.; Ludwig, T. Trace-element partitioning and boron isotope fractionation between white mica and tourmaline. *Can. Mineral.* **2011**, *49*, 165–176. [CrossRef]
65. Cook, N.J.; Ciobanu, C.L.; Meria, D.; Silcock, D.; Wade, B. Arsenopyrite-Pyrite Association in an Orogenic Gold Ore: Tracing Mineralization History from Textures and Trace Elements. *Econ. Geol.* **2013**, *108*, 1273–1283. [CrossRef]
66. Cabral, A.R.; Koglin, N. Hydrothermal fluid source constrained by Co/Ni ratios in coexisting arsenopyrite and tourmaline: The auriferous lode of Passagem, Quadrilátero Ferrífero of Minas Gerais, Brazil. *Mineral. Petrol.* **2012**, *104*, 137–145. [CrossRef]
67. Slack, J.F. Tourmaline associations with hydrothermal ore deposits. *Rev. Mineral.* **2002**, *33*, 559–644.
68. Henry, D.J.; Sun, H.T.; Slack, J.F.; Dutrow, B.L. Tourmaline in meta-evaporites and highly magnesian rocks: Perspectives from Namibian tourmalinites. *Eur. J. Mineral.* **2008**, *20*, 889–904. [CrossRef]
69. Lee, C.T.A.; Leeman, W.P.; Canil, D.; Li, Z.X. Similar V/Sc systematics in MORB and arc basalts: Implications for the oxygen fugacities of their mantle source regions. *J. Petrol.* **2005**, *46*, 2313–2336.
70. Wanty, R.B.; Goldhaber, M.B. Thermodynamics and kinetics of reactions involving vanadium in natural systems: Accumulation of vanadium in sedimentary rocks. *Geochim. Cosmochim. Acta* **1992**, *56*, 1471–1483. [CrossRef]
71. Liu, X.D.; Lu, X.C.; Wang, R.C.; Zhou, H.Q.; Xu, S.J. Speciation of gold in hydrosulphide-rich ore-forming fluids: Insights from first-principles molecular dynamics simulations. *Geochim. Cosmochim. Acta* **2011**, *75*, 185–194. [CrossRef]
72. Hofstra, A.H.; Cline, J.S. Characteristics and models for Carlin-type gold deposits. *Rev. Econ. Geol.* **2000**, *13*, 163–220.